Additive manufacturing of ZK60 magnesium alloy by selective laser melting: Parameter optimization, microstructure and biodegradability

C.L. Wu, Wei Zai, H.C. Man *

Department of Industrial and Systems Engineering, The Hong Kong Polytechnic University, Hung

Hom, Kowloon, Hong Kong, China

Abstract

Mg-Zn-Zr (ZK60) magnesium alloy samples were prepared by selective laser melting (SLM). The processability of ZK60 prepared by SLM was thoroughly investigated via varying the laser processing parameters. Experimental results show that laser power and scan velocity played an important role in determining the quality of SLM ZK60. SLM ZK60 with minimal defects and high dimensional accuracy could be obtained at a laser power of 50 W and scanning velocity of 500–800 mm/s. The formation mechanisms of pores were also identified and illustrated thoroughly in size and shape in the transition regimes. Significantly refined grains were observed in SLM ZK60, with an average grain size (G_a) of 7.3 μm for SLM ZK60 versus 56.4 μm for cast ZK60. Besides the α-Mg phase, the Mg_7Zn_3 eutectic phase was precipitated in the α-Mg matrix in SLM ZK60, and the MgZn phase in cast ZK60. The hardness of cast ZK60 and SLM ZK60 was 0.55 and 0.78 GPa, respectively, with similar elastic modulus. SLM ZK60 exhibited a higher corrosion resistance in Hanks' solution compared with cast ZK60 as indicated by a decrease of about 30% in hydrogen

---

* Corresponding author.
E-mail address: hc.man@polyu.edu.hk (H.C. Man)

evolution rate and of about 50% in the corrosion current density. The SLM ZK60 fabricated in the present study exhibits a great potential for biomedical applications due to desirable mechanical properties and a reasonably low degradable rate.

1. Introduction

Metallic materials, polymeric materials and ceramic materials are commonly used for orthopedic implants in clinical applications. Due to the low strength of polymeric materials and the high brittleness of ceramic materials, metallic biomaterials are more popular implant materials mainly on account of their combined strength and toughness [1-4]. Metallic materials such as stainless steel and titanium alloys have been used as key materials for decades in the biomedical fields, especially for orthopedic applications owing to their high strength and high corrosion resistance in human body environment [5, 6]. However, orthopedic implants made of stainless steel or Ti alloys will remain permanently inside the body after implantation, and permanent implants serve no purpose when healing is completed. On the contrary, its presence inside the body is a nuisance due to the shielding effect and release of toxic ions *in vivo* [7]. The shielding effect, which arises from the mismatch of the Young's modulus between the implant and natural bone, might eventually lead to osteopenia or even osteoporosis [8]. In view of this inherent drawback of conventional metallic

materials, a new generation of metal-based biocompatible materials with degradable property, such as biodegradable Mg and its alloys, offers a solution to the problem of requiring a second surgery for implant removal after recovery [9-11]. In comparison with stainless steel (189-205 GPa) and titanium alloys (110-117 GPa), Mg and its alloys have the lowest Young's modulus (41-45 GPa), being closest to that of the natural bone among the metallic materials [12-14]. Meanwhile, Mg ions can induce the formation of bone and shorten the healing time [15, 16]. However, the degradation rate of Mg and its alloys in body fluids is too high, which limits their biomedical applications [17]. Conventional manufacturing methods of Mg and its alloys are mainly based on deformation processing and casting [18, 19]. In particular, better mechanical properties could be obtained by deformation processing [18]. However, the slip of dislocations during the deformation only occurs on the basal plane (0001) and the direction $<1\bar{1}20>$, or the pyramidal plane $(1\bar{0}12)$ for the twining at room temperature owing to the nature of close-packed hexagonal structure, indicating a comparatively limited cold workability [20]. Orthopedic implants are difficult or impossible to fabricate by conventional manufacturing methods.

In view of these considerations, selective laser melting (SLM) offers a very attractive solution to the problem, which can directly build near net shaped component parts with complex geometry, requiring only little or even no post-machining [21-23]. However, studies on SLM of Mg alloys are scarcely reported in the literature due to the high vapor pressure of Mg, which makes SLM fabrication difficult. Ng et al. [14] reported fabrication of single-track pure Mg samples using

SLM. Zhang et al. [24] sintered a powder mixture of Mg-9%Al by SLM, and only a maximum relative density of 82% could be achieved. Wei et al. [25] successfully fabricated AZ91D magnesium alloys with nearly full-dense parts of approximate 99.52% relative density by SLM, and this particular SLM AZ91D magnesium alloy exhibited superior microhardness and tensile strengths at room temperature compared with the die-cast AZ91D. In addition to the capability of tailor-making, SLM is characterized by high melting/solidification rate with a cooling rate of above 10^5K/s, which could extend the solubility of alloying elements, refine the grain size and inhibit segregation. It has been reported that Mg alloys with small grain size and homogeneous microstructure have a lower degradation rate due to enhanced passivation and reduced microgalvanic attack [26, 27]. Argade et al. [26] demonstrated that the corrosion rate of the Mg-Y-RE alloys with ultrafine grain size was one order magnitude lower than that of the alloys with coarse grain size. Lu et al. [27] investigated the effects of intermetallic phases on the degradation behavior of Mg-3Zn alloys. This particular research revealed that Mg alloys exhibited a low degradation resistance when a large volume fraction of intermetallic phases were precipitated out. These studies suggest that SLM would be a promising method to manufacture Mg implants with favorable mechanical properties and improved corrosion resistance via optimal selection of laser processing parameters.

Previous studies have shown that Mg-Al binary and Mg-xAl-Zn ternary magnesium alloys exhibit excellent degradation resistance and good cytocompatibility, which are important for degradable orthopedic implants [28, 29]. It should be,

however, noticed that the Al elements in Mg alloys may impair bone mineralization and have an adverse effect on human neurons, and Al-containing Mg alloys are now gradually eliminated in implant applications [30]. On the other hand, Mg-Zn binary alloys show great potential in biodegradable implant materials due to their lower cytotoxicity compared with Al- or RE-containing Mg alloys [31]. In addition, Zn element is an essential element in human body and is crucial for biological function. However, the degradation rate of Mg-Zn alloys is undesirable in physiological environments, which can result in local intense alkalization and the formation of subcutaneous hydrogen bubbles. Therefore, the high degradation rate of Mg-Zn alloys is currently the biggest hurdle to be overcome. In addition, an implant is supposed to have patient-specific 3D profile and shape for best surgical outcomes. Additive manufacturing via SLM is an idea process for these purposes. Until now, studies on SLM of Mg alloys are scarcely reported in the literature due to the major issues such as insufficient fusion of powder, the high vapor pressure of Mg and the presence of large pores, which can be attributed to the results of poor understanding and process control during laser-powder interaction and melt pool solidification. In this paper, Mg-Zn-Zr (ZK60) magnesium alloy samples were prepared by SLM. The current study aims at (a) studying the processability of ZK60 prepared by SLM via varying the laser processing parameters; (b) exploring the formation mechanisms of pores and illustrating in size and shape in the transition regimes and (c) carrying out a comparative study on the microstructure, microhardness and biodegradation between SLM ZK60 and cast ZK60.

2. Materials and experimental details

2.1. Materials and specimen preparation

Mg-Zn-Zr alloying powders, namely ZK60, were used as the SLM materials and the chemical composition is shown in Table 1. Particle size distribution of the powders was measured using a laser diffraction particle size instrument (Malvern Mastersizer 2000, UK). The morphology and particle size distribution of the powders are shown in Fig. 1. These powders were spherical in shape as shown in Fig. 1 (a) and displayed an approximate Gaussian size distribution with median diameter of ~51 μm as shown in Fig. 1 (b).

Table 1

Chemical compositions of the raw ZK60 powder and SLM ZK60.

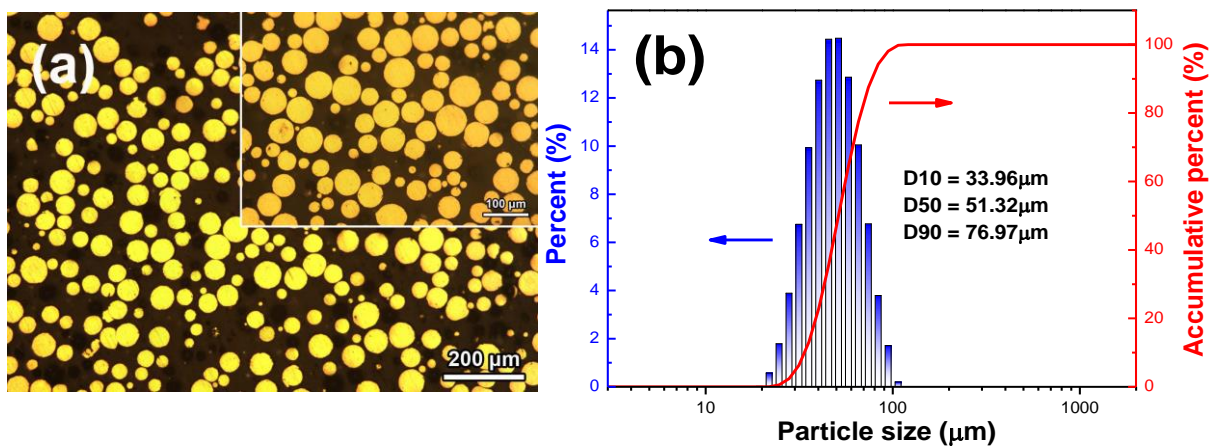| Samples	Mg (wt%)	Zn (wt%)	Zr (wt%)	Mg:Zn
ZK60 powder	94.5	5.2	0.3	18.2
SLM ZK60	95.4	4.6	0	20.7

Fig. 1. Cross-section morphology (a) and particle size distribution (b) of the ZK60 magnesium powders.

A commercial laser additive manufacturing system (SLM 125 HL, SLM Solutions, Germany) was used as the SLM equipment, which contains a CW fiber laser with a maximum output power of 400 W, an automatic powder supplying module, a building chamber with atmosphere control, a computer controlled multi-axis motion system and a workbench. Fig. 2 shows schematic diagram of the SLM process. The ZK60 powders were laid onto the surface of the substrate to form a powder bed and SLM was carried out according to the pre-set scanning path as shown in Fig. 2. When the nth layer of powders was melted, the workbench was moved down a distance of one layer and the scanning direction was rotated through 67° for the $(n+1)^{th}$ layer. By alternately repeating the scanning paths, a complete bulk sample with dimensions of 8 mm × 8 mm × 5 mm was obtained. During the SLM process, UHP argon gas was used to maintain a protective atmosphere with the oxygen content below 100 ppm in the building chamber. In addition, cast ZK60 magnesium alloy were also used for comparison.
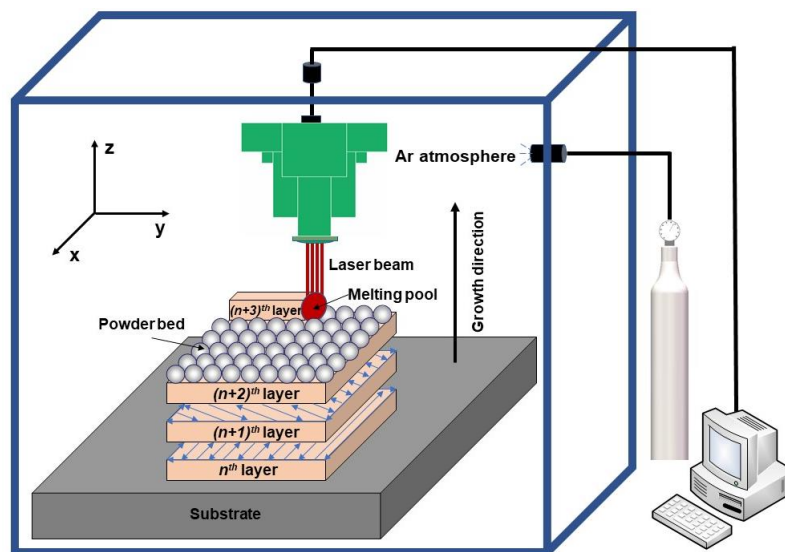

Fig. 2. Schematic diagram of the SLM process.

Additive manufacturing via SLM is an attractive processing technology for tailor making metallic parts. However, the selection of processing parameters is a challenging work because defects, such as pores and low relative density, are common in SLM parts. These are attributable to improper processing parameters, which result in incomplete melting (under-heating) or vaporization (overheating). Thus, optimization of processing parameters is of paramount importance and is the first step in successful SLM fabrication. To achieve optimization, sixty-four samples prepared by SLM with nominal dimensions of $8 \times 8 \times 5$ mm^3 (length $\times$ width $\times$ thickness, respectively) were obtained via varying laser powers and laser scan velocity, aiming at investigating the effect of processing parameters on the processability of SLM parts.

2.2. Microstructural analysis and microhardness measurement

Metallographic samples of cast ZK60 and SLM ZK60 were prepared by standard mechanical grinding and polishing procedures and were then etched in an etchant containing 6 g picric acid + 5 mL acetic acid + 100 mL ethanol +10 mL distilled water for microstructural observation. The surface morphology and chemical composition of the samples were studied using optical microscope (OM, Leica DMLM) and scanning-electron microscope (SEM, Tescan VEGA3) equipped with an energy dispersive spectrometer (EDS, Oxford Instrument). The porosity was measured by Image-Pro Plus 6.0 software. The phases formed in the samples were examined using X-ray diffractometer (XRD, Rigaku SmartLab) at a scanning speed of $2° \text{ min}^{-1}$, with

Cu Kα (λ = 1.5406 Å) radiation and generated at a voltage of 45 kV and a current of 200 mA, ranging from $2\theta = 10°$ to $100°$. The microhardness of the polished surface of the samples was measured using a Vickers hardness tester (HV, Mitutoyo MicroWizhard) with a load of 2 N and a duration time of 15 s. A minimum of seven measurements were performed for each sample to obtain the average microhardness value.

2.3. Degradation behavior

Electrochemical corrosion behaviors, including open-circuit potential (OCP) and potentiodynamic polarization (PDP) of cast ZK60 and SLM ZK60, were investigated by potentiodynamic polarization measurements (PARSTAT 2263) in Hanks' solution (pH = 7.4 ± 0.2) at 37 ± 0.5 °C. Samples with an exposed area of 0.8×0.8 cm^2 were embedded in epoxy resin and then polished successively with SiC abrasive papers up to 2000 grits for corrosion tests. A standard three-electrode system was used with a saturated calomel electrode (SCE) as the reference electrode, a platinum sheet as the auxiliary electrode, and the samples as the working electrode. Prior to PDP measurements, the samples were immersed for 1800 s in Hanks' solution to reach a stable OCP. After the OCP measurement, PDP measurement was performed at a scan rate of 1 mV/s, starting from a potential 500 mV below the OCP. The corrosion potential (E_{corr}) and corrosion current density (I_{corr}) were extracted from the PDP curves by Tafel extrapolation.

Immersion tests of cast ZK60 and SLM ZK60 were carried out to evaluate the degradation behaviors in Hanks' solution (pH = 7.4 ± 0.2) at 37 ± 0.5 °C for 7 days,

the exposed area being 0.8×0.8 cm^2. The volume of hydrogen generated from the samples was collected by a burette at regular intervals. Measurements of three replicates were performed for each type of sample to obtain the average hydrogen volume. In order to keep the solution fresh, the solution was refreshed every 24 h. The corrosion morphology and chemical composition of the samples after immersion were also characterized by SEM and EDS.

3. Results and discussion

3.1. Optimization of processing parameters

Fig. 3 shows the macro morphology of the SLM ZK60 samples in the x-y plane and the corresponding laser processing parameters used.
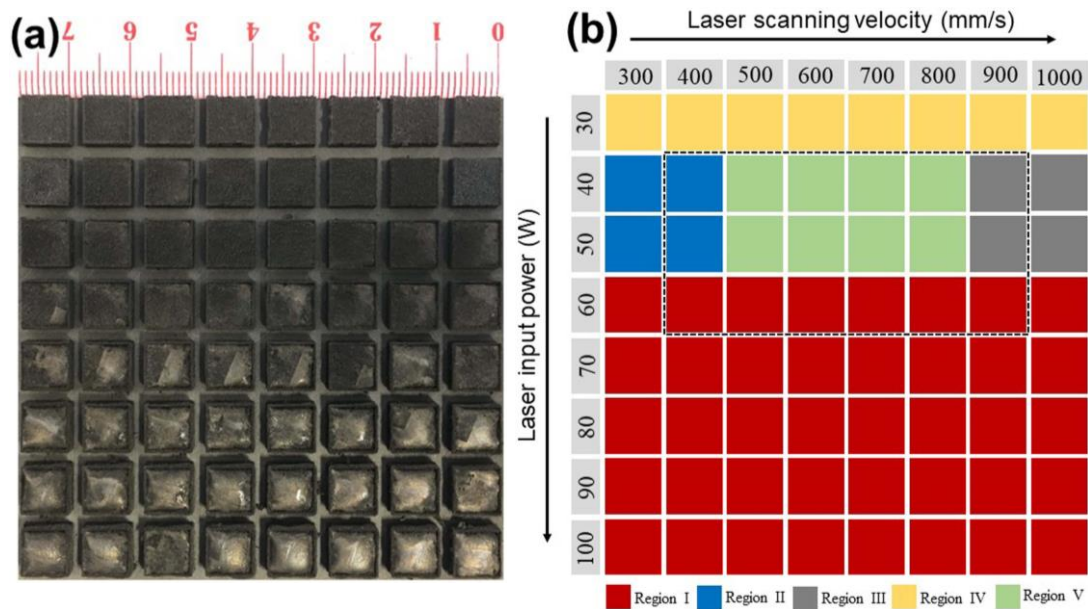

Fig. 3. Macro morphology of the SLM ZK60 magnesium alloys in the x-y plane (a) and the corresponding laser processing parameters used (b).

As can be seen from Fig. 3 (a), the processability of ZK60 during SLM depended on the laser input energy. Based on the morphology of the SLM samples, five groups of combinations of laser power and scanning velocity could be identified as shown in Fig. 3 (b). When the laser processing parameters were located in Region I, smoke were observed during SLM and the sample exhibited a non-uniform surface in addition to a low dimensional accuracy. The non-uniform surface and low dimensional accuracy of the samples resulted from the high input energy, and thus Region I is called the overheating region. The vapor pressure of magnesium is 0.13 kPa at 893 K and is dramatically increased to 51 kPa when the temperature is 1300 K [24]. An excess input energy could easily result in the evaporation of magnesium during continuous laser irradiation and make the metal molten splash due to the recoil pressure and Marangoni convection. As a consequence, samples with low dimensional accuracy were formed as the molten metal solidified while splashing occurred. By decreasing the laser input energy (Region II), evaporation was reduced and an improved surface quality was obtained. Nevertheless, samples still displayed low dimensional accuracy with relative non-uniform surface due to evaporation of magnesium, though less serious than in Region I. The input energy was further reduced in Region III. The samples obtained were relatively brittle, which can be attributed to the insufficient melting of the powder. The melting pool generated at low input energy had a small circumference-to-length ratio, leading to an unstable melting pool. Yadroitsev et al. [32] found that the scanning tracks were composed of discrete

droplets under this condition, deteriorating the formed quality of the samples. Under even lower laser power (Region IV), the SLM samples exhibited poor mechanical integrity. Meanwhile, some features of the original morphology of the powders can also be clearly observed on the surface of the samples. Region III and IV are called the under-heating region. When the processing parameters are located within the green region (Region V), with laser power of 40–50 W and scanning velocity of 500–800 mm/s, samples with uniform surface and optimal dimensional accuracy could be obtained, reflecting the input of an appropriate amount of laser energy. Thus Region V is called the forming region.

Fig. 4 shows the OM image at low magnification and porosity for SLM ZK60 in the x-y plane at laser power of 40–60 W and scanning velocity of 400–900 mm/s as marked by black-dotted rectangle in Fig. 3 (b).
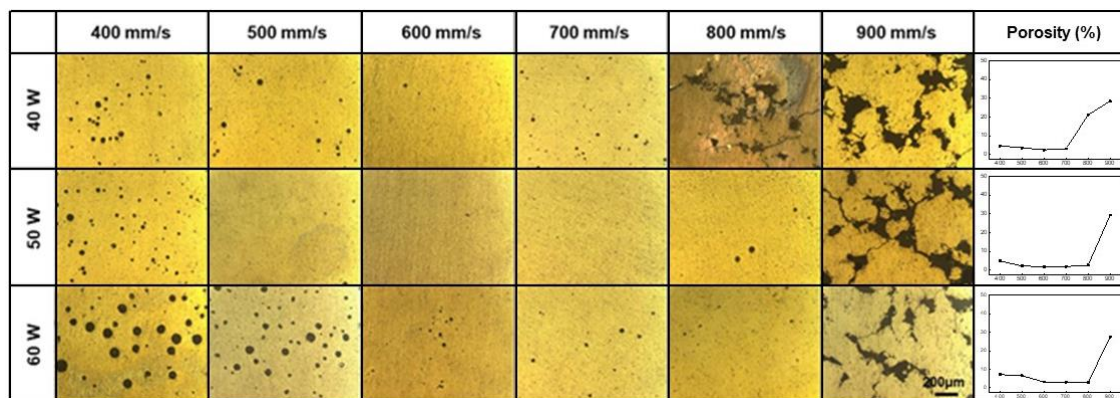

Fig. 4. OM image at low magnification and porosity for SLM ZK60 magnesium alloys in the x-y plane at laser power of 40–60 W and scanning velocity of 400–900 mm/s as marked by black-dotted rectangle in Fig. 3 (b).

As can be seen, the porosity decreased first and then increased with the increase of scanning velocity for a fixed value of laser power. In general, for a fixed scanning velocity, the porosity was significantly reduced at medium power (50 W) compared with the low power (40 W) and high power (60 W). On the one hand, it is worth noticing that the samples were covered with large amounts of irregular pores and these pores were connected to form a network at the upper right corner of Fig. 4 (low power and high scanning velocity). It has been reported that capillary instability would easily occur in the melting pool at a high scanning velocity, leading to formation of discrete droplets on the pool surface and the resulting balling effect [33]. The melting tracks with poor morphology were formed under this condition, which suppressed sufficient spreading of molten metal on the previously fabricated layer. Therefore, irregular pores would form due to insufficient overlapping between adjacent laser tracks and between adjacent layers. On the other hand, when the parameter combinations were located at the bottom left corner (high power and low scanning velocity) in Fig. 4, randomly dispersed pores with large spherical shapes were the primary defects in the samples. This phenomenon was attributed to keyhole effect generated at high laser power and low scanning velocity, leading to a deep melting pool with strong melting pool dynamics causing entrapment of vapor in pores as the melting pool propagated forward and the vapor cavity collapsed [34]. In addition, the keyhole mode porosity obviously increased at higher laser input energy because this would lead to a serious vapor cavity. Fig. 5 shows the formation mechanism of keyhole mode porosity. The keyhole mode is a severe instability regime,

which is one of the most important factors during the formation of pores. As shown in Fig. 5 (a), the bottom of the keyholes could be easily heated above the evaporation point of magnesium during laser irradiation because magnesium possesses a low boiling point and high vapor pressure. Hence, recoil pressure was dramatically increased and surface tension was decreased so that the keyholes were kept open at this point. However, the surface tension of the cooling local region in the upper region of the keyholes was increased, leading to shutting of the cooling local region and the appearance of the pores as shown in Fig. 5 (b). Meanwhile, the recoil pressure was increased again when the depression region was irradiated by the laser, and a strong downward flow formed below the depression region which would force the pores further back into the melting pool as shown in Fig. 5 (c). In general, the samples with minimum porosity of approximately 2.0% were obtained at a laser power of 50 W and scanning velocity of 500–800 mm/s, as shown in Fig. 4. This can be attributed to the fact that a relatively high laser input energy, but without evaporating magnesium, could reasonably decrease the dynamic viscosity of the molten metal, which would guarantee sufficient spreading of the molten metal and improve inter-layer wettability and consolidation [35]. Nevertheless, a small number of pores can still be observed in the samples, and these defects were still difficult to be completely eliminated in the SLM samples. The sample in following discussion was prepared at a laser power of 50 W and scanning velocity of 600 mm/s.
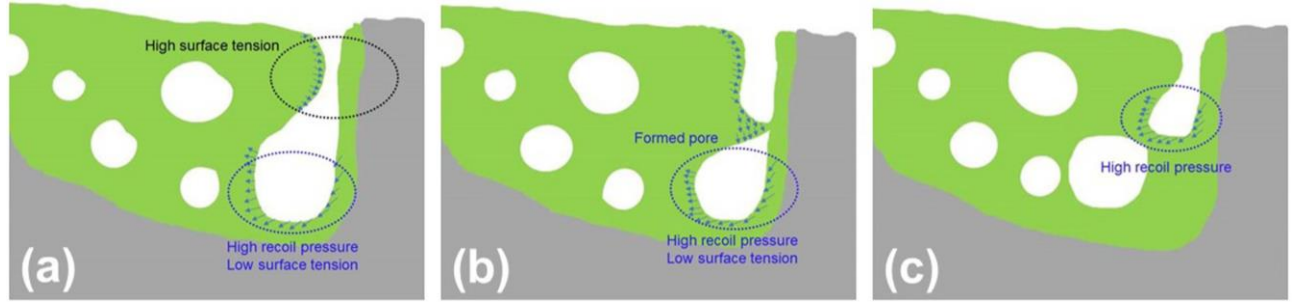
Fig. 5. Formation mechanism of keyhole mode porosity.

3.2. Microstructure and chemical composition

Fig. 6 shows the microstructure and EDS results of the precipitated phases for cast ZK60 and SLM ZK60. The average grain size (G_a) was determined via the intercept method according to the following equation [36]:

$$G_a = L/M\,N \tag{1}$$

where L is the length of measuring line, M is the magnification times and N is the number of grains crossed by the measuring line. The corresponding OM micrographs showing the grains are shown in Fig. 6 (a) and (b), and the average grain size G_a for cast ZK60 and SLM ZK60 was 56.4 μm and 7.3 μm, respectively. Therefore, the average grain size G_a of SLM ZK60 was much smaller than that of cast ZK60. The decrease in the grain size for the SLM ZK60 can be attributed to the high cooling rate characteristic of SLM. In addition, the alloying elements Zr and Zn, which act as grain refiner during solidification of the liquid melt, also played an important role in refining grains. The chemical composition of the SLM sample is also listed in Table 1. It is noticed that the Mg:Zn ratio for the raw powder and the SLM sample was 18.2 and 20.7, respectively, indicating a lower total content of Zn than the raw material. Wei et al. [9] also reported a similar result. Thus it might be commented that a small

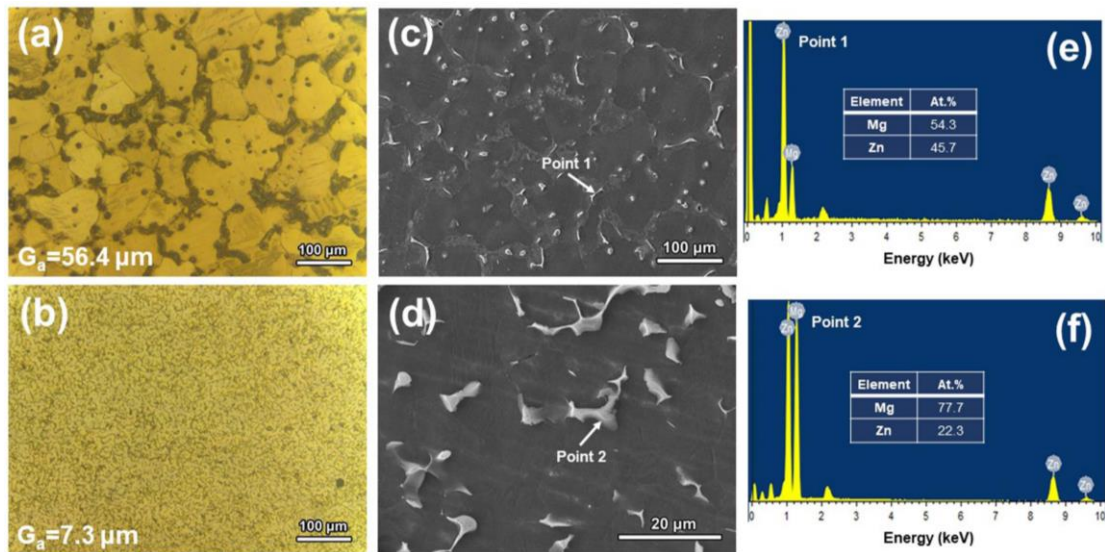change in the elemental composition is common in SLM.

Fig. 6. Microstructure of cast ZK60 (a), (c); SLM ZK60 (b), (d) and EDS results corresponding to point 1 (e) and point 2 (f).

Maxwell and Hellawell [37] reported that the growth restriction factor (GRF) can be used to evaluate the grain refinement efficacy of a solute, and the GRF for Zr and Zn solute is 38.29 and 5.31 in magnesium [38]. The combination of Zr and Zn solute exerts a significant grain refinement effect. During solidification, Zr solute serves as active sites for nucleation, contributing to the refinement of grain. Furthermore, Zn solute would also segregate in the diffusion layer ahead of the solid/liquid interface of a growing grain during constitutional undercooling and inhibit the growth of α-Mg grain. It is worth noticing that both cast and SLM ZK60 samples exhibited α-Mg matrix with equiaxed grains and precipitated phases, mainly found at grain boundaries as shown in Fig. 6 (c) and (d). The corresponding EDS results for locations marked as

point 1 and 2, indicate that these precipitated phases contained 54.3 at% Mg and 45.7

at% Zn in cast ZK60, and 77.7 at% Mg and 22.3 at% Zn in SLM ZK60 as shown in

Fig. 6 (e) and (f). No Zr element was found as its amount was too low to detect. These

EDS results suggest that the precipitated phases were mainly MgZn for cast ZK60 and

Mg_7Zn_3 for SLM ZK60, respectively. Fig. 7 shows the XRD patterns of cast ZK60
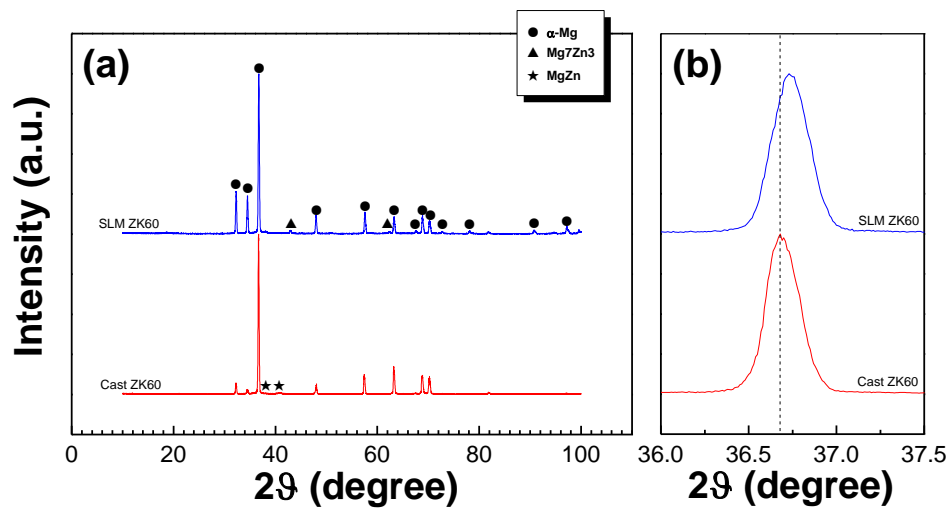
and SLM ZK60.

Fig. 7. XRD patterns of cast ZK60 and SLM ZK60 (a) and local XRD spectra within

$2\theta = 36°-37.5°$ (b).

Besides α-Mg phase with hcp structure, Mg_7Zn_3 eutectic phase for SLM ZK60 and

MgZn phase for cast ZK60 were precipitated out of α-Mg matrix, respectively. No

diffraction peaks corresponding to oxide inclusions such as MgO and ZnO appeared

in the SLM ZK60 sample due to the strict control of the content of O_2 and H_2O during

the SLM process. Fig. 8 shows the binary phase diagram of Mg-Zn.
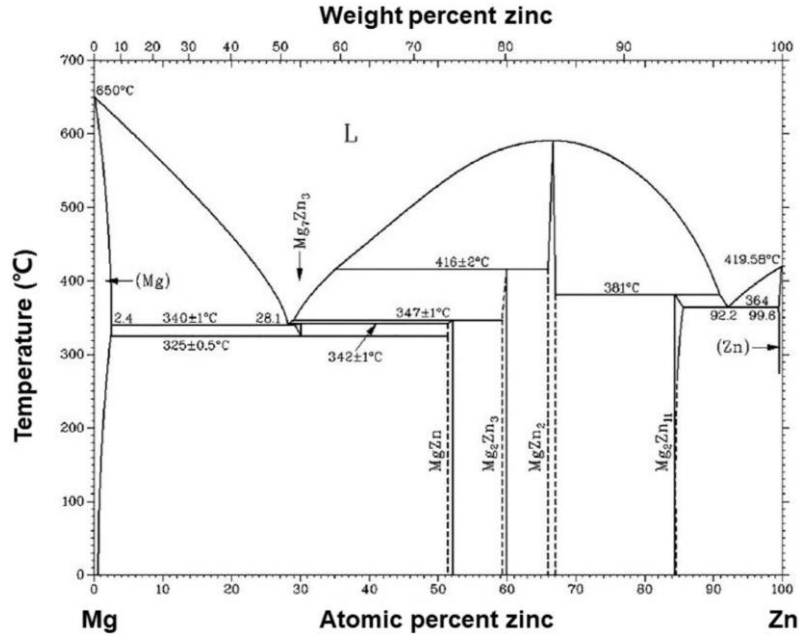
Weight percent zinc

Fig. 8. Binary phase diagram of Mg–Zn [39].

In theory, the eutectic reaction of the Mg-Zn alloy occurs from the liquid phase to form a mixture of α-Mg and Mg_7Zn_3 at 340 °C, and then the Mg_7Zn_3 eutectic phase for SLM ZK60 would be decomposed into α-Mg and MgZn phase at 325 °C via eutectoid reaction [39]. However, this decomposition ($Mg_7Zn_3 \rightarrow$ α-Mg + MgZn) is inhibited due to the high cooling rate of SLM. Therefore, the Mg_7Zn_3 phase was detected in SLM ZK60 sample and the MgZn phase appeared in cast ZK60 sample. Through a close-up view of the XRD patterns within $2\theta = 36°$-$37.5°$ as shown in Fig. 7 (b), the strong diffraction peaks of the α-Mg matrix for SLM ZK60 samples obviously shifted rightwards compared to that for cast ZK60. According to the Bragg's diffraction law [40]:

$$2d \sin \theta = n\lambda \qquad (2)$$

(where d is the interplanar spacing of the atomic lattice, θ is the angle between the

incident ray and the scattering planes, n is an integer ($n = $ 1, 2, 3…), λ is the wavelength of incident wave ($\lambda = $ 1.54060 Å for Cu K$_\alpha$ radiation)), the increase in the 2θ angle for the strong diffraction peaks of the α-Mg matrix can be attributed to the fact that Zn atoms acted as substitutive solutes in the α-Mg matrix based on the theory of solid solution, and the radius of Zn atoms (0.1187 nm) is smaller than that of Mg (0.1333 nm) [41]. In addition, the solid solubility of the α-Mg matrix was increased in rapid solidification in SLM [25]. As a consequence, a decrease of the interplanar spacing and a distortion of lattice structure would occur for SLM ZK60, leading to an increase in diffraction angles compared to cast ZK60.

3.3. Mechanical property

The Vickers microhardness of pure Mg, cast ZK60 and SLM ZK60 was 0.25, 0.55 and 0.78 GPa, with the microhardness of SLM ZK60 much higher than that of pure Mg and cast ZK60, showing a remarkable increase by 212% and 41.8%, respectively. This could be mainly attributed to grain boundary strengthening effect, which could be estimated by the Hall-Petch equation for polycrystalline materials [14]:

$$H_g = H_0 + kd^{-1/2} \tag{3}$$

where H_g is the hardness of material, H_0 and k are appropriate constants associated with the hardness measurements, d is the mean grain size. The hardness is inversely proportional to the square root of the grain size as shown in the equation (3). The strengthening mechanism of grain refinement is mainly attributed to the grain

boundaries acting as obstacles during dislocations motion.

Elastic modulus is a quantity that measures materials resistance to being deformed elastically when a stress is applied to it. In orthopedic implants a high elastic modulus could result in stress shielding effect, which eventually led to bone loss and loosening of implants. For magnesium alloys, alloying or heat treatment plays a negligible role in elastic modulus [42]. Thus the elastic modulus of pure Mg, cast ZK60 and SLM ZK60 could be assumed to be similar. Fig. 9 shows the comparison of hardness and elastic modulus of pure Mg, cast ZK60 and SLM ZK60 with natural bone and conventional metallic implant materials. As can be seen, the hardness and elastic modulus of pure Mg, cast ZK60 and SLM ZK60 were much closer to those of natural bone compared with conventional metallic implant materials such as Ti-based alloy, stainless steel and Co-Cr alloy. Therefore, the "stress shielding" effects can be significantly reduced by the use of Mg-based alloy implants.
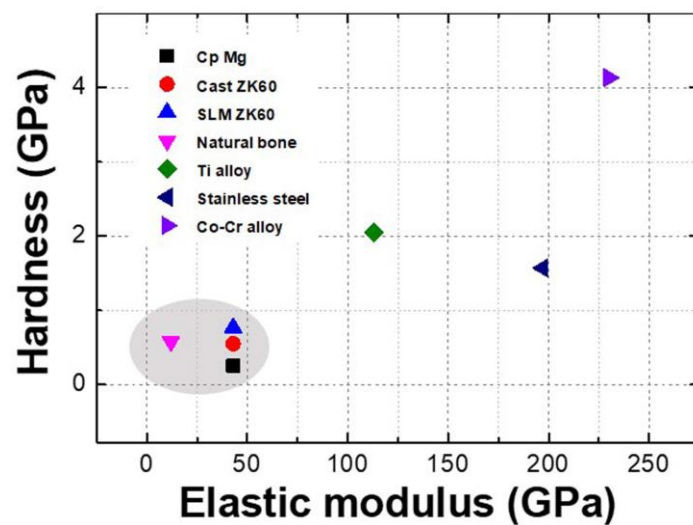

Fig. 9. Comparison of hardness and elastic modulus of pure Mg, cast ZK60 and SLM ZK60 with natural bone and conventionally metallic implant materials [12-14, 43].

3.4. Corrosion properties in Hanks' solution

Fig. 10 shows potentiodynamic polarization curves obtained in Hanks' solution at 37 °C for cast ZK60 and SLM ZK60. The corrosion parameters including corrosion potential (E_{corr}) and corrosion current density (I_{corr}) were extracted by Tafel fitting and are summarized in Table 2. Compared with those of cast ZK60, SLM ZK60 sample exhibited a higher corrosion resistance as indicated by a lower I_{corr} of 8.89 $\mu A/cm^2$ with a nobler E_{corr} of -1.52 V vs. SCE. In addition, the cathodic current density of SLM ZK60, controlled by hydrogen evolution reaction, was relatively lower than that of cast ZK60, indicating a lower hydrogen evolution rate of SLM ZK60. On the anodic branch, it is noticed that current density of SLM ZK60 was also lower in comparation with the cast ZK60 at the same potential, implying the decrease in anodic dissolution rate for SLM ZK60. Based on the I_{corr} (mA cm^{-2}), the corrosion rate P_i (mm/year) can be calculated as following [44]:

$$P_i = 22.85 \, I_{corr} \tag{4}$$

The corrosion rate P_i was calculated according to equation (4) and results are listed in Table 2. The corrosion rate P_i for cast ZK60 and SLM ZK60 was 0.42 and 0.2 mm/year, indicating that the corrosion resistance of SLM ZK60 was higher than that of cast ZK60.
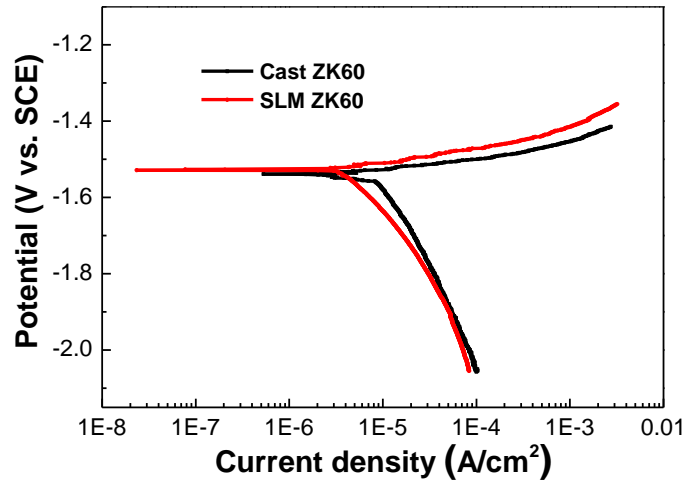
Fig. 10. Potentiodynamic polarization curves obtained in Hanks' solution at 37 ℃

for cast ZK60 and SLM ZK60.

Table 2

Polarization parameters and corrosion rate P_i for cast ZK60 and SLM ZK60 obtained

in Hanks' solution at 37 ℃.

Samples	E_{corr} (V vs. SCE)	I_{corr} ($\mu A/cm^2$)	P_i (mm/year)
Cast ZK60	-1.55	18.5	0.42
SLM ZK60	-1.52	8.89	0.20

To further investigate the corrosion properties, the degradation behaviors in

Hanks' solution were thoroughly analyzed. Fig. 11 shows the hydrogen evolution rate

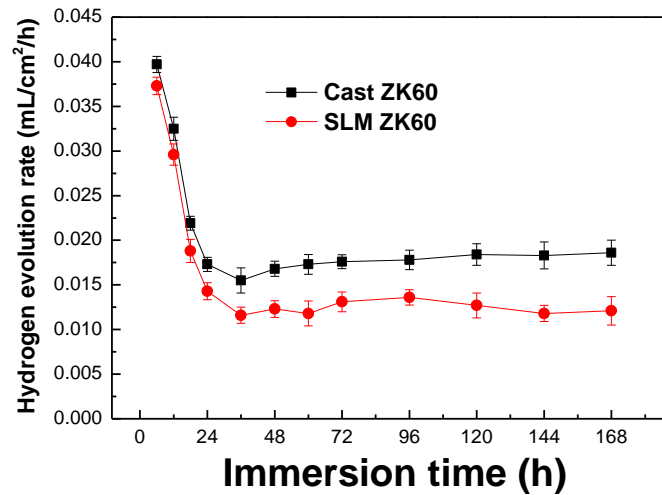as a function of immersed time for cast ZK60 and SLM ZK60.

Fig. 11. Hydrogen evolution rate as a function of immersed time for cast ZK60 and

SLM ZK60.

The hydrogen evolution rate results shown in Fig. 11 indicate that the cast ZK60

and SLM ZK60 exhibited a rapid hydrogen evolution rate at the beginning of

immersion. The hydrogen evolution rate decreased with the increase of immersion

time due to the formation of corrosion product layer. The rate for SLM ZK60 was

smaller than that of cast ZK60 by about 30%. These results indicate a better corrosion

resistance of SLM ZK60 as compared with cast ZK60. Gu and Li et al. [31] and Shuai

et al. [45] have also reported that cast ZK60 exhibited a higher corrosion rate than

refine-grained ZK60 magnesium alloys. When the Mg alloy samples are immersed in

Hanks' solution, the degradation of Mg alloys results in the release of OH^- ions,

leading to the formation of $Mg(OH)_2$. The formed $Mg(OH)_2$ can act as a moderately

protective layer. However, $Mg(OH)_2$ is unstable, offers low corrosion resistance, and

would break down easily, especially in chloride-containing environments (Hanks'

solution). According to the corrosion results shown in Fig. 10 and Fig. 11, there is a

good agreement between the corrosion resistance determined by electrochemical corrosion test and immersion corrosion test, confirming that SLM ZK60 sample exhibited a higher corrosion resistance. Kirkland et al. [46] reported that the Pilling-Bedworth ratio of Mg was below 1, indicating that the compressive stress of oxide layer for Mg was relatively high and thus cracks would be easily formed. However, the SLM ZK60 samples with refined grains possessed a high amount of grain boundaries, which indicated that compressive stress was reduced because of partial elimination of the oxide/matrix metal mismatch [29]. Therefore, the integrity of the oxide film was improved and could partially hinder the chloride ions from attacking the samples. It has also been reported [45, 47, 48] that the corrosion resistance can be improved through grain refinement. The hot-rolled AZ31 alloy [49] and a hot-extruded Mg–Ca alloy [50] alloy also exhibited an improved corrosion resistance due to the grain refinement during the forming processing. The strong Marangoni convection and the following solution capture effect during SLM would contribute to the formation of a more homogeneous microstructure in SLM60. Thus, uniform corrosion rather than localized corrosion would occur when an alloy possesses a homogeneous microstructure because segregation is minimized. Fig. 12 shows the typical corrosion morphology and the corresponding EDS results of cast ZK60 and SLM ZK60. The corrosion products on the immersion surfaces of cast ZK60 and SLM ZK60 show obvious cracks, which can be attributed to dehydration of the corrosion products [29]. As shown in Fig. 12 (a), cast ZK60 exhibits a rough surface with flaking of corrosion products, indicating serious corrosion attack. As for

the SLM ZK60 shown in Fig. 12 (b), the corrosion product layer is much intact and compact. The EDS results in Fig. 12 (c) and (d) reveal corrosion products enriched in O, Mg, P and Ca, indirectly indicating a good hydroxyapatite-forming ability.
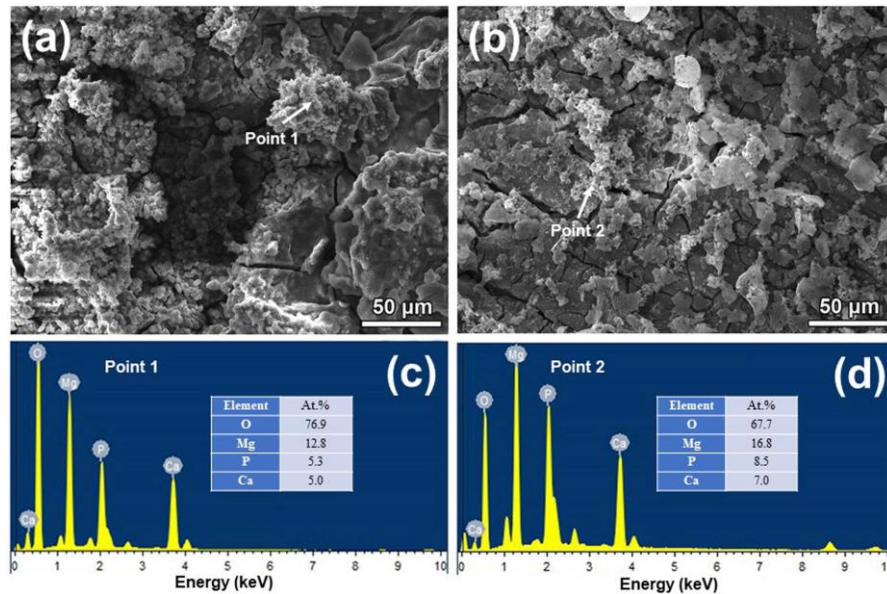

Fig. 12. Typical corrosion morphology and the corresponding EDS result of cast ZK60 (a), (c) and SLM ZK60 (b), (d).

4. Conclusions

In this work, different combinations of laser processing parameters were employed to prepared SLM ZK60 magnesium alloy samples, aiming at fabricating samples with minimal defects and improved dimensional accuracy. Furthermore, the formation mechanisms of pores were identified in different processing regimes. The corrosion behavior of SLM ZK 60 samples in Hanks' solution was compared with the cast samples. The main conclusions as are follows:

(1) The quality of SLM ZK60 directly depended on laser powers and scan velocity.

SLM ZK60 with minimal defects and improved dimensional accuracy could be obtained at laser power of 50 W and scanning velocity of 500–800 mm/s.

(2) The average grain size G_a for cast ZK60 and SLM ZK60 was 56.4 μm and 7.3 μm, respectively. The decrease in the grain size for the SLM ZK60 can be attributed to the high cooling rate resulting from characteristic of SLM.

(3) The Vickers hardness of cast ZK60 and SLM ZK60 in present work was 0.55 and 0.78 GPa, with similar elastic modulus. The hardness and elastic modulus of SLM ZK60 was the closest to those of natural bone compared with conventional metallic implant materials, such as Ti-based alloy, stainless steel and Co-Cr alloy.

(4) SLM ZK60 exhibited a higher corrosion resistance as indicated by a lower I_{corr} of 8.89 μA/cm^2 as compared with 18.5 μA/cm^2 for cast ZK60, and also a 30% decrease in hydrogen evolution rate.

These findings in mechanical and corrosion properties indicate that the SLM ZK60 fabricated in the present study exhibits a great potential for orthopedic applications due to its desirable mechanical properties and low degradation rate.

CRediT authorship contribution statement

C.L. Wu: Methodology, Investigation, Data curation, Writing - original draft. **Wei Zai**: Methodology, Investigation. **H.C. Man**: Conceptualization, Funding acquisition, Methodology, Formal analysis, Writing - review & editing, Supervision.

Disclosure statement

The authors declare that they have no known competing financial interests or personal relationships that could have appeared to influence the work reported in this paper.

References

[1] S. Jin, D. Zhang, X.P. Lu, Y. Zhang, L.L. Tan, Y. Liu, Q. Wang, Mechanical properties, biodegradability and cytocompatibility of biodegradable Mg-Zn-Zr-Nd/Y alloys, J. Mater. Sci. Technol. 47 (2020) 190–201.

[2] M. Sikora-Jasinska, P. Chevallier, S. Turgeon, C. Paternoster, E. Mostaed, M. Vedani, D. Mantovani, Understanding the effect of the reinforcement addition on corrosion behavior of Fe/Mg2Si composites for biodegradable implant applications, Mater. Chem. Phys. 223 (2019) 771–778.

[3] S. Loffredo, C. Paternoster, N. Giguère, G. Barucca, M. Vedani, D. Mantovani, The addition of silver affects the deformation mechanism of a twinning-induced

plasticity steel: Potential for thinner degradable stents, Acta Biomater. 98 (2019) 103–113.

[4] S. Vazirian, A. Farzadi, Dissimilar transient liquid phase bonding of Ti-6Al-4V and Co-Cr-Mo biomaterials using a Cu interlayer: Microstructure and mechanical properties, J. Alloys Compd. 829 (2020) 154510.

[5] A. Ataee, Y.C. Li, D. Fraser, G.S. Song, C Wen, Anisotropic Ti-6Al-4V gyroid scaffolds manufactured by electron beam melting (EBM) for bone implant applications, Mater. Des. 137 (2018) 345–354.

[6] X.C. Yan, Q. Li, S. Yin, Z.Y. Chen, R. Jenkins, C.Y. Chen, J. Wang, W.Y. Ma, R. Bolot, R. Lupoi, Z.M. Ren, H.L. Liao, M. Liu, Mechanical and in vitro study of an isotropic Ti6Al4V lattice structure fabricated using selective laser melting, J. Alloys Compd. 782 (2019) 209-223.

[7] M.H. Wong, H.C. Man, Low-temperature fabrication of Ag-doped HA coating on NiTi, Mater. Lett. 229 (2018) 229–231.

[8] C.W. Chan, H.C. Man, T.M. Yue, Susceptibility to stress corrosion cracking of NiTi laser weldment in Hanks' solution, Corros. Sci. 57 (2012) 260–269.

[9] K.W. Wei, Z.M. Wang, X.Y. Zeng, Influence of element vaporization on formability, composition, microstructure, and mechanical performance of the selective laser melted Mg–Zn–Zr components, Mater. Lett. 156 (2015) 187–190.

[10] N. Pulido-Gonzalez, B. Torres, S. García-Rodríguez, P. Rodrigo, V. Bonache, P. Hidalgo-Manrique, M. Mohedano, J. Rams, Mge1Zne1Ca alloy for biomedical applications. Influence of the secondary phases on the mechanical and corrosion

behaviour, J. Alloys Compd. 831 (2020) 154735.

[11] D. Bian, W.R. Zhou, Y. Liu, N. Li, Y.F. Zheng, Z.L. Sun, Fatigue behaviors of HP-Mg, Mg–Ca and Mg–Zn–Ca biodegradable metals in air and simulated body fluid, Acta Biomater. 41 (2016) 351–360.

[12] A. Biesiekierski, J. Wang, M.A.H. Gepreel, C Wen, A new look at biomedical Ti-based shape memory alloys, Acta Biomater. 8 (2012) 1661–1669.

[13] J.L. Li, L.L. Tan, P. Wan, X.M. Yu, K. Yang, Study on microstructure and properties of extruded Mg–2Nd–0.2Zn alloy as potential biodegradable implant material, Mater. Sci. Eng. C 49 (2015) 422–429.

[14] C.C. Ng, M.M. Savalani, M.L. Lau, H.C. Man, Microstructure and mechanical properties of selective laser melted magnesium, Appl. Surf. Sci. 257 (2011) 7447–7454.

[15] N. Sezer, Z. Evis, S.M. Kayhan, A. Tahmasebifar, M. Koç, Review of magnesium-based biomaterials and their applications, J. Magnes. Alloy. 6 (2018) 23–43.

[16] Y. Xin, T. Hu, P.K. Chu, *In vitro* studies of biomedical magnesium alloys in a simulated physiological environment: A review, Acta Biomater. 7 (2011) 1452–1459.

[17] Y. Zheng, Magnesium alloys as degradable biomaterials, CRC Press, 2015.

[18] B.Q. Xiao, J.F. Song, A.T. Tang, B. Jiang, W.Y. Sun, Q. Liu, H. Zhao, F.S. Pan, Effect of pass reduction on distribution of shear bands and mechanical properties of AZ31B alloy sheets prepared by on-line heating rolling, J. Mater. Process.

Technol. 280 (2020) 116611.

[19] S.K. Woo, C. Blawert, K.A. Yasakau, S. Yi, N. Scharnagl, B.C. Suh, Y.M. Kim, B.S. You, C.D. Yim, Effects of combined addition of Ca and Y on the corrosion behaviours of diecast AZ91D magnesium alloy, Corros. Sci. 166 (2020) 108451.

[20] H.T. Teng, X.L. Zhang, Z.T. Zhang, T.J. Li, S. Cockcroft, Research on microstructures of sub-rapidly solidified AZ61 Magnesium Alloy, Mater. Charact. 60 (2009) 482–486.

[21] D. Carluccio, A.G. Demir, L. Caprio, B. Previtali, M.J. Bermingham, M.S. Dargusch, The influence of laser processing parameters on the densification and surface morphology of pure Fe and Fe-35Mn scaffolds produced by selective laser melting, J. Manuf. Process. 40 (2019) 113–121.

[22] C.A. Biffi, A.G. Demir, M. Coduri, B. Previtali, A. Tuissi, Laves phases in selective laser melted TiCr1.78 alloys for hydrogen storage, Mater. Lett. 226 (2018) 71–74.

[23] C.C. Ng, M.M. Savalani, H.C. Man, I. Gibson, Layer manufacturing of magnesium and its alloy structures for future applications, Virtual Phys. Prototyp. 5 (2010) 13–19.

[24] B.C. Zhang, H.L. Liao, C. Coddet, Effects of processing parameters on properties of selective laser melting Mg-9%Al powder mixture, Mater. Des. 34 (2012) 753–758.

[25] K.W. Wei, M. Gao, Z.M. Wang, X.Y. Zeng, Effect of energy input on formability, microstructure and mechanical properties of selective laser melted AZ91D

magnesium alloy, Mater. Sci. Eng. A 611 (2014) 212–222.

[26] G.R. Argade, S.K. Panigrahi, R.S. Mishra, Effects of grain size on the corrosion resistance of wrought magnesium alloys containing neodymium, Corros. Sci. 58 (2012) 145–151.

[27] Y. Lu, A.R. Bradshaw, Y.L. Chiu, I.P. Jones, The role of β_1 precipitates in the bio-corrosion performance of Mg-3Zn in simulated body fluid, J. Alloys Compd. 614 (2014) 345-352.

[28] C.J. Shuai, C.X. He, L. Xu, Q. Li, T. Chen, Y.W. Yang, S.P. Peng, Wrapping effect of secondary phases on the grains: increased corrosion resistance of Mg–Al alloys, Virtual Phys. Prototyp. 13 (2018) 292–300.

[29] C.J. Shuai, C.X. He, P. Feng, W. Guo, C.D. Gao, P. Wu, Y.W. Yang, S.Z. Bin, Biodegradation mechanisms of selective laser-melted Mg–xAl–Zn alloy: grain size and intermetallic phase, Virtual Phys. Prototyp. 13 (2018) 59–69.

[30] M. Niinomi, Recent research and development in titanium alloys for biomedical applications and healthcare goods, Sci. Technol. Adv. Mater. 4 (2003) 445–454.

[31] X.N. Gu, N. Li, Y.F. Zheng, L.Q. Ruan, *In vitro* degradation performance and biological response of a Mg–Zn–Zr alloy, Mater. Sci. Eng. B 176 (2011) 1778–1784.

[32] I. Yadroitsev, A. Gusarov, I. Yadroitsava, I. Smurov, J. Mater. Process. Technol. 210 (2010) 1624–1631.

[33] N.T. Aboulkhair, N.M. Everitt, I. Ashcroft, C. Tuck, Reducing porosity in AlSi10Mg parts processed by selective laser melting, Addit. Manuf. 1 (2014)

77–86.

[34] A.D. Plessis, Effects of process parameters on porosity in laser powder bed fusion revealed by X-ray tomography, Addit. Manuf. 30 (2019) 100871.

[35] D. Gu, Y.C. Hagedorn, W. Meiners, K. Wissenbach, R. Poprawe, Nanocrystalline TiC reinforced Ti matrix bulk-form nanocomposites by Selective Laser Melting (SLM): Densification, growth mechanism and wear behavior, Compos. Sci. Technol. 71 (2011) 1612–1620.

[36] Y.W. Yang, P. Wu, X. Lin, Y. Liu, H. Bian, Y.Z. Zhou, C.D. Gao, C.J. Shuai, System development, formability quality and microstructure evolution of selective laser-melted magnesium, Virtual Phys. Prototyp. 11 (2016) 173–181.

[37] I. Maxwell, A. Hellawell, A simple model for grain refinement during solidification, Acta Metall. 23 (1975) 229–237.

[38] Y. Lee, A. Dahle, D. StJohn, The role of solute in grain refinement of magnesium, Metall. Mater. Trans. A 31 (2000) 2895–2906.

[39] H. Okamoto, Comment on Mg-Zn (magnesium-zinc), J. Phase Equilib. 15 (1994) 129–130.

[40] Y. Zhou, G. Wu, Analysis Methods in Materials Scienced X-ray Diffraction and Electron Microscopy in Materials Science, Harbin Institute of Technology Press, Harbin, 2007.

[41] C. Suresh, N. Koga, A consistent approach toward atomic radii, J. Phys. Chem. A 105 (2001) 5940–5944.

[42] D.L. Shu, Mechanical property of engineering materials, China Machine Press,

2nd, 2007.

[43] V.H. Pham, S.H. Lee, Y.L. Li, H.E. Kim, K.H. Shin, Y.H. Koh, Utility of tantalum (Ta) coating to improve surface hardness in vitro bioactivity and biocompatibility of Co-Cr, Thin Solid Films 536 (2013) 269–274.

[44] R. Xu, M.C. Zhao, Y.C. Zhao, L. Liu, C. Liu, C.D. Gao, C.J. Shuai, A. Atrens, Improved biodegradation resistance by grain refinement of novel antibacterial ZK30-Cu alloys produced via selective laser melting, Mater. Lett. 237 (2019) 253–257.

[45] C.J. Shuai, Y.W. Yang, P. Wu, X. Lin, Y. Liu, Y.Z. Zhou, P. Feng, X.Y. Liu, S.P. Peng, Laser rapid solidification improves corrosion behavior of Mg-Zn-Zr alloy, J. Alloys Compd. 691 (2017) 961–969.

[46] N.T. Kirkland, N. Birbilis, M.P. Staiger, Assessing the corrosion of biodegradable magnesium implants: a critical review of current methodologies and their limitations. Acta Biomater. 8 (2012) 925–936.

[47] N. Birbilis, K.D. Ralston, S. Virtanen, H.L. Fraser, C.H.J. Davies, Grain character influences on corrosion of ECAPed pure magnesium, Corros. Eng. Sci. Technol. 45 (2010) 224–230.

[48] G.R. Argade, S.K. Panigrahi, R.S. Mishra, Effects of grain size on the corrosion resistance of wrought magnesium alloys containing neodymium, Corros. Sci. 58 (2012) 145–151.

[49] H. Wang, Y. Estrin, Z. Zúberová, Bio-corrosion of a magnesium alloy with different processing histories, Mater. Lett. 62 (2008) 2476–2479.

[50] Z.J. Li, X. N. Gu, S. Q. Lou, Y. F. Zheng, The development of binary Mg-Ca alloys for use as biodegradable materials within bone, Biomaterials 29 (2008) 1329–1344.